X-691-72-418
PREPRINT
NASA TM X- 66088

CROSS SECTIONS FOR PRODUCTION OF THE CO($A^1\Pi$-$X^1\Sigma$) FOURTH POSITIVE BAND SYSTEM AND O(^{3}S) BY PHOTODISSOCIATION OF CO_2

E. P. GENTIEU
J. E. MENTALL

NOVEMBER 1972

GODDARD SPACE FLIGHT CENTER
GREENBELT, MARYLAND

CROSS SECTIONS FOR PRODUCTION OF THE $CO(A^1\Pi\text{-}X^1\Sigma)$ FOURTH POSITIVE BAND SYSTEM AND $O(^3S)$ BY PHOTODISSOCIATION OF CO_2

By

E. P. Gentieu and J. E. Mentall

Laboratory for Extraterrestrial Physics
NASA-Goddard Space Flight Center
Greenbelt, Maryland 20771

Excitation cross sections were measured for producing $CO(A^1\Pi)$ by photodissociation of CO_2 from threshold to 635Å. Above 685Å the $CO(A^1\Pi)$ cross section is of the order 1×10^{-18} cm^2 and exhibits considerable structure while below 685Å the $CO(A^1\Pi)$ cross section rapidly drops to a nearly constant value of $\sim 3 \times 10^{-19}$ cm^2. The structure below 790Å correlates with predissociation from known Rydberg states of CO_2 demonstrating the competition between preionization and predissociation. An upper limit of 6% of the $CO(A^1\Pi)$ cross section was inferred for producing $O(^3S)$. Although not directly observed, evidence was obtained that the production of $CO(A^1\Pi)$ is accompanied by production of $O(^1D)$ and $O(^1S)$ at incident photon wavelengths less than 800 and 700Å respectively. The $CO(A^1\Pi\text{-}X^1\Sigma)$ vibrational intensity distribution was obtained with 7Å resolution for 16.69 eV photon impact and is similar to a 20 eV electron impact produced distribution.

I. INTRODUCTION

Observations of the Mars upper atmosphere via the Mariner 6, 7, and 9 spacecraft have unearthed further interest in the interaction of neutral CO_2 with far UV photons. The Martian atmosphere consists almost entirely of CO_2 and analysis of the Mariner ultraviolet spectrometer data[1,2] imputes strong emissions in the $CO(A^1\Pi - X^1\Sigma)$, $CO(a^3\Pi - X^1\Sigma)$, $CO_2^+(\tilde{A}^2\Pi-\tilde{X}^2\Sigma)$, and $CO_2^+(\tilde{B}^2\Sigma-\tilde{X}^2\Sigma)$ molecular band systems to excitation of ambient CO_2 molecules by photons and photoelectrons. There is a considerable volume of literature[3-14] dealing with electron and photon excitation of CO_2. However, with the exception of Cook et al's.[3] observations of CO_2^+ fluorescence and Lawrence's[6] measurement of $CO(a^3\Pi-X^1\Sigma)$ Cameron band cross sections, previous photodissociative excitation studies [3-6] have been made using only a few spectral lines for excitation. A detailed analysis of the Mariner results requires cross sections determined with a continuum excitation source over the entire wavelength interval that the integral of the cross section over the solar spectrum has appreciable magnitude. With these goals in mind we report here cross sections for producing the $CO(A^1\Pi-X^1\Sigma)$ Fourth Positive (CO 4 PG) band system and the O(1304) resonance transition from the following photodissociative mechanisms:

$$\begin{aligned} CO_2(\tilde{X}^1\Sigma_g^+) + h\nu &\rightarrow CO_2^* \quad \lambda < 919\text{Å}. \\ CO_2^* &\rightarrow CO(A^1\Pi) + O(?) \\ CO(A^1\Pi) &\rightarrow CO(X^1\Sigma^+) + \Sigma_{v',v''} h\nu(v',v'') \end{aligned} \tag{1}$$

and

$$CO_2(\tilde{X}^1\Sigma_g^+) + h\nu \rightarrow CO_2^* \qquad \lambda < 829\text{Å}$$

$$CO_2^* \rightarrow CO(X^1\Sigma^+) + O^* \qquad (2)$$

$$O^* \rightarrow O(^3P) + h\nu\ (1304\text{Å}).$$

The O atom in Reaction (1) may be in either the ^3P, ^1S, or ^1D state depending on the energy of the incident photon and the emitted photons may result from cascade processes.

Cross sections for mechanisms (1) and (2) were obtained by passing the dispersed radiation from a continuum background lamp through a column of CO_2 and viewing the CO 4PG fluorescence radiation with two solar blind photomultipliers located at right angles to the incident photon beam. One of the phototubes was preceded by a 1mm-thick BaF_2 window so that the O(1304) emission could be separated from the CO 4PG emissions. Relative cross sections were measured as a function of incident photon energy from threshold to 636Å and were put on an absolute basis by comparing the CO fluorescence signal with an H Lyman-α signal of known cross section, obtained from 839Å photon impact on molecular hydrogen. Due to the smallness of the O(1304) cross section the results for mechanism (2) represent only an upper limit.

Using a second experimental apparatus similar to that of Wauchop and Broida,[8] we obtained the CO 4PG relative intensity distribution produced by 744Å photon impact on CO_2. The photon produced distribution was compared for heuristic considerations to a 20 $\pm$ 2 eV electron impact produced distribution using the same

apparatus and resolution. Additionally, this apparatus was used to obtain relative measurements of cross sections for producing O(1304) and $CO(A^1\Pi)$ by both 744Å and 584Å photon impact on CO_2.

II. EXPERIMENTAL

The apparatus is shown schematically in Fig. 1. Details of the background photon source and its method of excitation are described elsewhere.[15,18] Light from the Hopfield continuum lamp was dispersed to a measured bandpass of 0.5Å by a one-meter McPherson 225 monochromator. Attached to the exit slit of the monochromator was a 52-cm-long stainless steel absorption chamber viewed at one end by a sodium salicylate coated photomultiplier tube. Two EMR 541G solar blind photomultipliers, one of which was preceded by a 1-mm-thick BaF_2 window, were located 11 cm from the exit slit, at right angles to the axis of the absorption chamber. The effective band pass of the tube sans BaF_2 window was 1060-1850Å while the BaF_2 window limited the short wavelength response of the second tube to 1365Å. Thus one tube saw $CO(A^1\Pi - X^1\Sigma)$ transitions from v' levels up to 18 plus O(1304) while the second tube was limited to viewing $A^1\Pi - X^1\Sigma$ transitions from $v' \leq 5$ or 6. The 541 G tubes were hooked up in a photon counting configuration with the semi-transparent photocathodes grounded to insure that electrostatic fields did not penetrate the interaction region of the absorption cell. The outputs of these tubes fed a pair of Hewlett Packard 5554 charge sensitive preamplifiers which were discriminated and then counted by a pair of Hamner NS-11 preset scalers slaved to a Hamner NT-11 preset timer. Since

the fluorescence signal was weak (0.2 to 3 counts per second) the scaler-timer combination allowed counting either for uniform statistics when the signal exceeded about 0.7 cts per second or for a fixed 10 min period. Most of the data displayed in Fig. 3 represents counting accuracies of 3 to 6%. The 6% figure applies to the region from 850Å to threshold and from 636 to 690Å where the fluorescence signal was limited by low incident photon intensities. Two one hour dark counting periods preceded each 8 to 16 hour experimental run. Over the 6 month period during which we collected data the dark counts of the two tubes varied from 0.1 to 0.3 counts per second but were stable to about 10% over a given days data run. The upward gain drift phenomenon[19] was investigated in the solar blind tubes and was found to be $< 5\%$ over a 10 minute data collection period.

The sodium salicylate coated photomultiplier was operated in an analog mode and was attached to a Keithley 417 picoammeter. Pressure in the absorption chamber was monitored with an MKS Baratron capacitance manometer. A 2^{19} shaft position encoder attached to the wavelength drive of the monochromator read the position of the monochromator drive with a resolution of 0.01Å. The outputs of both the picoammeter and the pressure gauge were digitized by an EECO 762 analog to digital converter and then passed along with the digital information from the scalers, timers, and shaft encoder readout through a digital multiplexer into an IBM 1800 process control computer. The

computer operated in a closed loop with a stepping motor attached to the monochromator drive and after data at a particular wavelength had been collected and processed the wavelength drive was automatedly advanced, the electronics reset, and a new data collection cycle initiated. Data collection periods were limited mainly by erosion of the electrodes in the spark gap which triggered the incident photon source and by clogging of the entrance slit by erosion processes in the lamp itself. Generally, the light source could only be operated for 12 to 16 hours before the entrance slit required cleaning.

Since it was not feasible to make measurements of the incident intensity, $I_o(\lambda)$, during an experimental run, we used the transmitted intensity, $I(\lambda)$, measured by the salicylate coated phototube and previously determined total absorption cross sections, $\sigma_t(\lambda)$, to calculate $I_o(\lambda)$ at each data collection point. Total absorption and photoionization cross sections measured by Nakata et al.[7] were chosen based upon the review by Hudson,[20] the experience of Lawrence,[6] and agreement between Nakata's results and our own measurements made from 910 to 925Å. We further observed that the structure in our transmitted intensity measurements compared very favorably with the structure in Nakata's measurements of σ_t. The wavelength scale of Nakata's data vis. a vis. ours was also examined for discrepancies using troughs in our I measurements and peaks in the σ_t values as criteria for alignment. A small ($\pm$ 0.3Å) systematic deviation between the two scales was sometimes found throughout a given nights data run. We attribute this deviation to uncertainty in

fixing an absolute reference point for our wavelength readout.[21] Where such deviations were noted our scale was adjusted to more closely coincide with the wavelength observations of Nakata which in turn are in good agreement above 700Å with high resolution photographic assignments.[22]

Research grade CO_2 was used throughout the experiment without further purification. Data were taken at pressures which varied between 4 and 20 millitorr. No pressure dependence of the fluoresence signal was observed over this pressure range. The CO_2 flowed through the absorption cell and out the slit of the monochromator at a rate such that the chamber was entirely refreshed every 2 seconds.

III. CALIBRATION

Under steady state conditions the number of CO 4PG photons created in an element of pathlength dl along the axis of the absorption chamber in the field of view of the solar blind detectors can be expressed as

$$\int_o^\infty I_f(\lambda,\lambda') \, d\lambda' = N\sigma_f(\lambda) I_o(\lambda) \exp(-\sigma_t(\lambda) NL) \, dl \quad , \qquad (3)$$

where $I_f(\lambda,\lambda')$ denotes that the $CO(A^1\Pi\text{-}X^1\Sigma)$ vibrational intensity distribution is a function of both the wavelength of the incident photon, λ, and the wavelength of the emitted photon, λ', $\sigma_t(\lambda)$ is the CO_2 total absorption cross section, N is the CO_2 number density, $I_o(\lambda)$ is the incident photon intensity at the beginning of the fluorescence detector field of view and L is the axial length of the field of view. In the case where the solid angle subtended by dl at the detector varies negligibly across L, Eq. (3) can be integrated across the field of view of the detectors and solved for $\sigma_f(\lambda)$ to give

$$\sigma_{f(\lambda)} = \frac{\sigma_t(\lambda) \int_o^\infty I(\lambda,\lambda') \, d\lambda'}{I_o(\lambda) \, [1-\exp(-\sigma_t(\lambda) NL)]} \quad . \qquad (4)$$

In evaluating Eq. (4) the parameters we have empirical access to are the fluorescence signal generated by the solar blind detector

$$S_f(\lambda) = K_f \int I_f(\lambda,\lambda') \, Q_f(\lambda') d\lambda', \qquad (5)$$

and the signal produced by the salicylate coated phototube which monitored the transmitted intensity at the end of the absorption chamber

$$S_s(\lambda) = K_s Q_s(\lambda)\ I_o(\lambda)\ \exp(-\sigma_t(\lambda)NX). \qquad (6)$$

In these expressions K_f and K_s are constants related to gain and geometry factors, $Q_f(\lambda')$ is the quantum efficiency of the solar blind detectors, $Q_s(\lambda)$ is the quantum efficiency of the sodium salicylate coating, and X is the distance along the chamber axis between the salicylate coating and the onset of the field of view of the fluorescence detectors. Eqs. (5) and (6) can be substituted into Eq. (4) to obtain $\sigma_f(\lambda)$.

In the cross section measurements there was not sufficient signal to disperse the 4PG emissions and thus empirically determine the $I(\lambda,\lambda')$ of Eq. (6) at each incident wavelength. $I(\lambda,\lambda')$ was determined with 7.5Å resolution for 744Å photon impact on CO_2 in a corollary experiment using a neon resonance lamp and an apparatus similar to Wauchop and Broida.[8] This technique is identical to that used to study VUV electron impact excitation cross sections[23] except that a resonance lamp preceded by a thin aluminum window replaces the electron gun. The $I(744Å,\lambda')$ thus obtained was used to weight the quantum efficiency of the solar blind detectors over the fluorescence intensity distribution via:

$$\bar{Q} \simeq \frac{\int_{1300\text{Å}}^{1850\text{Å}} I(744\text{Å},\lambda')\, Q(\lambda')\, d\lambda'}{\int_{1300\text{Å}}^{1850\text{Å}} I(744\text{Å},\lambda')\, d\lambda'} \qquad (7)$$

The limits on the definite integrals in Eq. (7) represent the limits of our measurements of $I(744\text{Å},\lambda')$. In the case of the tube which was preceded by the BaF_2 window, the integral in the numerator of Eq. (7) also included the measurement transmission of the window. $Q_f(\lambda')$ was determined by calibrating the solar blind detectors against a secondary standard photodiode calibrated at the National Bureau of Standards. Both solar blind tubes were calibrated relative to their respective quantum efficiencies at 1216Å in roughly 25Å intervals between 1150 and 2100Å using the Goddard Space Flight Center triple beam optical calibration facility. Dispersed radiation from a dc discharge in H_2 generated the $I_o(\lambda')$ used in calibrating the tubes. Data was taken at nearly constant $I_o(\lambda')$ values and after a fixed period of illumination of the solar blind photocathodes in order to minimize errors caused by gain drifts. The results of eight calibration runs were averaged and are estimated to have an absolute accuracy of 12%.

The experimentally determined $\bar{Q}(744\text{Å})$ will differ significantly from the true $\bar{Q}(\lambda)$ where only the first few v' levels can be excited. Comparison of the $\bar{Q}$ computed for 744Å incident radiation (which can excite $CO(A^1\Pi)$ vibrational levels up to v'= 23 depending on the state of the oxygen fragments) and a calculated $\bar{Q}$ assuming only v'=0 was excited produced a 25% difference. We estimate that when v' = 2 is also populated this deviation will decrease to less than 10%. As subsequent v' levels are populated $\bar{Q}(744\text{Å})$ should rapidly approach $\bar{Q}$ (true).

Relative $CO(A^1\Pi)$ cross section data from 635 to 925Å were placed on an absolute basis by comparing the CO 4PG fluorescence signal to an H(1216Å) signal obtained from 839.2Å photon impact on molecular hydrogen. Excitation cross sections for the latter process have been measured by Mentall and Gentieu[15] and by Comes and Wenning[16,17] who observe that $H_2 + h\nu(\lambda = 839.2\text{Å}) \rightarrow H(2s) + H(1s)$ with a quantum yield of nearly unity. For ambient H_2 pressures exceeding 6 millitorr approximately 70% of the H(2s) atoms are converted via collisions to H(2p) with the consequent emission of a 1216Å photon.[15] At any incident wavelength the ratio of the CO fourth positive fluorescence cross section to the H Lyman-α cross section at λ = 839Å is obtained by combining Eqs. (4), (5), (6), and (7) which gives:

$$\frac{\sigma_f(CO_2)}{\sigma_f(H_2)} = \frac{\sigma_t(CO_2)}{\sigma_t(H_2)} \cdot \frac{Q_f(1216)}{\bar{Q}} \cdot \frac{Q_s(\lambda)}{Q_s(839)} \cdot \frac{S_f(CO_2)}{S_f(H_2)} \cdot \frac{S_s(H_2)}{S_s(CO_2)} \qquad (8)$$

$$\cdot \frac{\exp(\sigma_f(H_2)N(H_2)X) - \exp(\sigma_t(H_2)N(H_2)(X-L))}{\exp(\sigma_t(CO_2)N(CO_2)X) - \exp(\sigma_t(CO_2)N(CO_2)(X-L))} \cdot$$

In evaluating Eq. (8) we have assumed $Q_s(\lambda)/Q_s(839) = 1$.[24] The factor $Q_f(1216)$ in Eq. 8 enters as a result of the H(1216Å) signal and cancels with a like factor implicit in $\bar{Q}$ leaving the result independent of Q at 1216Å. In placing the $CO(A^1\Pi)$ cross sections on an absolute scale we measured the H_2 total absorption cross section at 839.2Å with 0.5Å resolution, assumed 100% dissociation[15-17] at 839.2Å and then used the data from Fig. 5 of reference 15 to compute $\sigma_f(H_2, 839.2Å)$. The calibration was effected by substituting H_2 for CO_2 in the absorption chamber under identical conditions of gain and collection geometry of the fluorescence detectors. This calibration was carried out after each days data run to insure that aging effects in the sodium salicylate coating of the incident beam monitor did not introduce excessive errors.

V. RESULTS AND DISCUSSION

A. Relative Intensity Distributuon and $O(^3S)$ Cross Sections.

Fig. 2 shows the $CO(A^1\Pi - X^1\Sigma)$ vibrational intensity distribution produced by photodissociative excitation of CO_2 at 743Å. Shown for comparison is a spectrum excited by 20 ±2 eV electrons. For levels with v' = 0, 1 and 2 the vibrational populations are quite similar while for v' ≥ 4 the photon produced distribution becomes progressively hotter. The OI(1302-4-6Å) multiplet is also considerably enhanced in the photon induced spectra. Using the absolute cross section for $CO_2 + 743Å \rightarrow CO(A^1\Pi) + O$ from our broad band measurements (Section VB) and the ratio of the area under the O(1304) peak to the total area in the photon distribution gives an O(1304) cross section of $(1.0 \pm .5) \times 10^{-20}$ cm^2 at 743Å. The O(1304) cross section was also measured at 584Å and found to be $< 10^{-21}$cm^2. Below 21 eV the most probable channel for production of $O(^3S)$ is a cascade process:[25]

$$CO_2(\tilde{X}^1\Sigma_g^+) + h\nu \rightarrow CO(X^1\Sigma_g^+) + O(2p^3 3p^3P). \qquad (9)$$

$$O(2p^3 3p^3P) \rightarrow O(2p^3 3s^3S) + 8447Å$$

$$O(2p^3 s^3S) \rightarrow O(2p^4\ ^3P) + 1304Å$$

Direct production of $CO(X^1\Sigma_g^+) + O(^3S)$ is not an important mechanism for production of O(1304) since it implies a $CO_2(^3\Sigma^-)$ intermediate state which violates the $\Sigma^+ \not\leftrightarrow \Sigma^-$ selection rule.[26]

The O(1304) cross section as a function of incident wavelength can be obtained by substracting the signals of the two solar blind detectors observing the fluorescence photons or equivalently by examining

the ratio of these signals. After correcting for the difference in band pass for 4PG emissions introduced by the BaF_2 window, we observe that the O(1304) cross section does not exceed the statistical noise (~6%) in the measurements. We conclude that from threshold to 636Å $\sigma_f(O^3S)/\sigma_f(CO(A^1\Pi) \leq 0.06$.

It is interesting to compare the distributions of figure 2 to the 20 eV electron impact laboratory distribution (taken at 10Å resolution) which appeared in the Mariner 6 and 7 UV spectrometer report.[1] Considering the difference in resolution the intensity distributions are in fair agreement except that we observe no carbon lines. Barth et al. suggest that the carbon 1561 and 1657Å multiplets can be produced by electron impact on CO_2 at 20 eV, i.e.:

$$CO_2 + e \rightarrow C(3s\ ^3P^o\ ) + O_2(X^3\Sigma_g^-) + e \qquad 18.97\ eV$$

and

$$CO_2 + e \rightarrow C(2s2p^3\ ^3D^o) + O_2(X^3\Sigma_g^-) + e \qquad 19.43\ eV$$

both of which imply highly bent intermediate states. With 7.5Å resolution, the C(1561) multiplet is overlapped by the (1,1) and (4,3) 4PG bands at 1560.1 and 1559.5Å while the C(1657) multiplet is overlapped by the 4PG (0,2) band at 1653.5Å. A second electron impact spectrum was therefore obtained with an electron energy of 24 ± 2 eV and with 0.3Å resolution. Neither the C(1561) nor the C(1657) multiplets were observed. We conclude that these multiplets are produced with a significant cross section only through the total dissociation of CO_2 viz.

$$CO_2 + e \rightarrow C(3s\ ^2P^o) + 2\ O(2p^4\ ^3P) + e \qquad 24.05\ eV$$

$$\rightarrow C(2s\ 2p^3\ ^3D^o) + 2\ O(2p^4\ ^3P) + e \qquad 24.51\ eV$$

as was suggested by the earlier work of Mumma.[11]

B. $CO(A^1\Pi)$ Cross Sections

Fig. 3 and Table I exhibit the $CO(A^1\Pi)$ excitation cross sections, $\sigma_f(\lambda)$, as a function of incident energy from threshold to 636Å. Shown for comparison in Fig. 3 are $\sigma_t(\lambda)$, $\sigma_i(\lambda)$ and $\sigma_d(\lambda)$ measured by Nakata et al.[7] Thresholds for various competing channels are indicated along the top of the figure. Most of the data represent the average of at least two sets of measuremmets. The threshold for producing CO 4PG was observed to be 925Å, corresponding to excitation of $CO(A^1\Pi, v'=0)$ from $CO_2(\tilde{X}^1\Sigma_g^+)$ at a rotational temperature of 300°K. For wavelengths longer than 802.5Å the only channel available for $CO(A^1\Pi)$ production is $CO_2 + h\nu \rightarrow CO(A^1\Pi) + O(^3P)$. This mechanism is in violation of the spin selection rule. However, violation of the spin rule has been observed by Inn and Heimerl[27] in photodissociatively produced $CO(X^1\Sigma_g^+) + O(^3P)$. Intermediate coupling in CO_2^* leading to $CO(A^1\Pi) + O(^3P)$ for the case of electron impact on CO_2 has recently been discussed by Krauss[28] et al. Intermediate coupling can also lead to violation of spin conversation in photon produced 4PG and results in $CO(A^1\Pi)$ yields which are rather low above 800Å. A singlet-singlet mechanism, $CO_2 + h\nu \rightarrow CO(A^1\Pi) + O(^1D)$, becomes energetically possible at 802.5Å and a second singlet channel, $CO_2 + h\nu \rightarrow CO(A^1\Pi) + O(^1S)$, occurs at 702Å. Other possible mechanisms shortwards of 802Å involve cascade from higher lying singlet states: CO_2 $h\nu \rightarrow CO(B^1\Sigma^+$ or $C^1\Sigma^+) + O(^3P)$, with thresholds at 763.3Å and 735.3Å. Thresholds for $CO(B^1\Sigma^+$ or $C^1\Sigma^+) + O^1D$ occur at 680.8Å and 658.8Å respectively, however, the $CO(A^1\Pi)$ cross section is very small in this region and the cascade mechanism accompanied by O^1D production is unimportant.

The $CO(A^1\Pi)$ cross section is maximum at 900Å, falling off to a minimum of 2×10^{-19} cm^2 at about 835Å. Structure in the region between 875 and 899Å is apparently non-Rydberg in nature and cannot be correlated with known series or progressions in the CO_2 total absorption spectrum. However, shortwards of 850Å there is nearly a complete correspondence between structure in the $CO(A^1\Pi)$ cross section and structure in the dissociation and ionization cross sections as measured by Nakata et al.[7] The region between 790 and 840Å is characterized by weak bands overlapping a continuum. Bands in this region have been classified as Progressions I and II by Tanaka et al.[29]

The intense structure in the $CO(A^1\Pi)$ cross section below 790Å can be attributed to predissociation out of two series of Rydberg states converging respectively to $CO_2^+(\tilde{A}^2\Pi_u)$ and $CO_2^+(\tilde{B}^2\Sigma_u^+)$. Using the wavelength assignments of Tanaka and Ogawa[22] we observe T-O Rydberg series in the $CO(A^1\Pi)$ cross section converging to v' = 1-6 of CO_2^+ $(A^2\Pi_u)$ and also the Henning (s) series converging to $CO_2^+(\tilde{B}^2\Sigma_u^+)$. The Henning (d) series may also be present but cannot be unambiguously identified. The n = 8 and 9 members are not apparent in our data and n = 3-7 members are overlapped by strong bands belonging to T-O series or progressions. We note that below about 790Å every feature in the $CO(A^1\Pi)$ cross section is Rydberg in nature. Moreover, the total absorption cross section and all of the partial cross sections, σ_i, σ_{pd}, and σ_f

which have been studied to date follow the same series of Rydberg states demonstrating the competition between preionization and predissociation in this region.

Below 686Å, the series limit corresponding to $CO_2(\tilde{B}^2\Sigma_u^+)$, the $CO(A^1\Pi)$ cross ection falls off rapidly to a constant 3×10^{-19} cm^2 out to the limit of our continuous measurements at 636Å. We also determined the fourth positive cross section at 584Å to be $< 10^{-20} cm^2$.

A question of interest is whether or not singlet spin mechanisms compete strongly with the triplet mechanism at wavelengths shorter than 802Å. Unfortunately the metastable $O(^1D)$ and $O(^1S)$ states are unobservable at the signal levels involved in our experiment. However, we can qualitatively identify their presence by examining the CO 4PG signal for vibrational cooling near the thresholds for the singlet processes. This was accomplished by plotting the mean ratio of the two solar blind detectors in 6-12Å wavelength intervals as a function of incident photon energy. The transmission of the BaF_2 window preceding one of the solar blind detectors decreased continuously from 1800Å and cut off completely at about 1367Å. One would therefore expect the ratio of $S_{Bare}(\lambda)/S_{BaF_2}(\lambda)$ to continually increase as higher vibrational levels are populated (i.e., as the incident photon wavelength decreases). Figure 4 shows a histogram of the mean ratio of the detectors as a function of incident photon wavelength from 695-850Å. The wavelength intervals of the histogram have been selected to correspond to calculated thresholds for the mechanisms

shown. Additionally, all thresholds have been adjusted upward by .07 eV to account for initial thermal excitation in the parent CO_2 molecule. We interpret the dips in the histogram at the thresholds for $CO(A^1\Pi) + O(^1S)$ or $O(^1D)$ as evidence of vibrational cooling in the $CO(A^1\Pi - X^1\Sigma)$ intensity distribution which implies that 4PG emissions are being produced from a competing channel with lower v' levels. We also observe a small decrease corresponding to the threshold for production of $CO(B^1\Sigma^+)$. However, since the branching ratio for $CO(B^1\Sigma^+) \rightarrow CO(X^1\Sigma^+)$ is large (approximately .85)[30] and since the $CO(B^1\Sigma - X^1\Sigma)$ system lies at shorter wavelengths than the 4PG, one should actually see an increase in the histogram if any sizable amount of $CO(B^1\Sigma^+)$ was being produced.

The fraction of the CO 4PG intensity due to the onset of the singlet channels can be estimated from the data in Fig. 4 by assuming that the quantum efficiencies of the fluorescence detectors are uniform over the intensity distribution. If it is further assumed that the partial fluorescence cross section due to the triplet channel is constant across the $O(^1D)$ threshold the break in Fig. 4 at 800Å corresponds to an increase of 40-80% in the production rate of vibrationally cold $CO(A^1\Pi)$. This result is inconsistent with the data of Fig. 2 which show at most only a 20-30% change in the fluorescence cross section at the $O(^1D)$ threshold. This implies that production of $CO(A^1\Pi)$ via the singlet channel occurs at the expense of the triplet channel as would be the case if the initial absorption is to a bound state of CO_2 which then predissociates into either a singlet or into a triplet channel. A second calculation based on a model which assumes the total fluorescence cross section

is constant across the singlet thresholds again suggests that at least 50% of the fluorescence cross section occurs through the singlet channels.

C. Fractional Yield

Figure 5a shows total and dissociation yields for photons on CO_2 leading to $CO(A^1\Pi)$ production as a function of incident photon energy from 636 to 925Å. The data of Nakata[7] et. al. for CO_2 total and photodissociation cross sections have been used to compute the yields. In the uppermost curve the yields have been computed on a point for point basis by first fitting a curve to Nakata's data and then interpolating values for σ_i and σ_{pd} at each point that a fourth positive cross section was determined. The yields computed in this manner can be seen to exhibit considerable structure and are not continuous through any of the CO_2^+ ionization limits as was observed by Lawrence[6] for photodissociatively produced $CO(a^3\Pi)$. We are not certain how to interpret the marked increase in structure and magnitude in the dissociation yeild shortwards of 765Å. Nakata et al. report their ionization cross sections are perhaps low at the sharp peaks in the total absorption cross section in this region which would tend to increase resultant photodissociation cross sections and thus depress the dissociation yield. However, σ_i is of the same order as σ_f and at least some of the structure in the yields can be attributed to a combination of

error in σ_{pd},[33] a 0.2Å difference in resolution between Nakata's data and our data, and to random errors in the wavelength scales. The increase in structure does coinside with the threshold for producing $CO(B^1\Sigma^+) + O(^3P)$ which could then populate $CO(A^1\Pi)$ by cascade. We cannot rule out the cascade mechanism since an alternative interpretation of the increase (below 760Å) in the ratio of the two fluorescence signals displayed in Fig. 4 is production of $CO(B^1\Sigma)$. However, the $CO(B^1\Sigma - X^1\Sigma)$ branching ratio is so large[30] that a $CO(B^1\Sigma)$ yield of nearly unity would be required to significantly populate the $CO(A^1\Pi)$ state via. cascade. Since $CO_2(X^1\Sigma^+) + h\nu \rightarrow CO(B^1\Sigma^+) + CO(^3P)$ is spin forbidden such a large yield for this channel seems quite unlikely though not impossible.

The bottom half of Fig. 5 shows the yields obtained by integrating across corresponding features in the antecedent σ_f, σ_{pd}, and σ_t curves. This method of data reduction alleviates resolution and random wavelength errors but also smooths physically real structure where the area under the peaks is less than or comparable to the area in the apparent underlying continuum, The resultant data (Fig. 5B) is strongly smoothed above 760Å but still exhibits an increase in structure and magnitude below 760Å. From threshold to 850Å the behavior of the yield curves in 5B is similar to that reported by Lawrence[6] for Cameron Band production. Lawrence computed his yield curves in a manner similar to that used to obtain 5b but in both cases the "modus reductum datum" competes with physical reality as explanation of

the ensuing smoothness in the branching ratios making it difficult to give meaningful interpretation to the result. Leaving aside the question of structure in the yields we note that the magnitude of the $CO(A^1\Pi)$ dissociation yield is in correspondence with the $CO(a^3\Pi)$ yield reported by Lawrence. When normalized to Nakata's data the sum of the two cross sections account for (70 ± 25)% of Nakata's dissociation cross section in the region where the two measurements overlap.

D. DISCUSSION OF ERRORS

Table II summarizes the uncertainties present in our measurements. Over modest wavelength intervals except where $CO(A^1\Pi)$ v' = 0 thresholds occur, the relative accuracy of the $CO(A^1\Pi)$ cross sections given in Table I is about 25%. Over the entire range of the measurements the relative accuracy is 50 to 60%. This decrease in relative accuracy results mainly from the first two items in Table II. The absolute calibration adds 20% uncertainty at any point. The graphs in Figure 2 and 5 were obtained by linear interpolation between data points taken in .25 or .50Å intervals which may result in interpolation errors where the $CO(A^1\Pi)$ structure is sharp.

CONCLUSIONS

The $CO(A^1\Pi)$ cross sections reported here, along with previously determined electron impact results, establish the basis for calculating CO Fourth Positive System volume emission rates in the Martian dayglow.[31] Calculated volume emission rates will in turn determine the relative contribution of photon vs electron impact as mechanisms for producing $CO(A^1\Pi)$ in the Mars atmosphere. The smallness of the O(1304) cross section confirms previous indirect evidence[32] that photodissociative excitation of CO_2 is not an important source of $O(^3S)$ in the upper atmosphere of Mars.

ACKNOWLEDGMENTS

We wish to thank M. J. Mumma for a thoughtful criticism of the manuscript and William Mish for assistance in some of the programming.

35

REFERENCES AND FOOTNOTES

1. C. A. Barth, C. W. Hord, J. B. Pearse, K. K. Kelley, G. P. Anderson and A. I. Stewart, J. Geophys. Res., 74, 2213, (1971).
2. C. A. Barth, C. W. Hord, A. I. Stewart, and A. L. Lane, Science, 175, 309, (1972).
3. G. R. Cook, P. H. Metzger, and M. Ogawa, J. Chem. Phys., 44, 2935, (1966).
4. K. D. Beyer and K. H. Welge, Z. Naturforsch 19a, 19, (1964).
5. D. L. Judge and L. C. Lee, J. Chem. Phys. (in press).
6. G. M. Lawrence, J. Chem. Phys., 56, 3435, (1972).
7. R. S. Nakata, K. Watanabe, and F. M. Matsunaga, Science of Light, 14, 54, (1965).
8. T. S. Wauchop and H. P. Brodia, J. Geophys. Res., 76, 21, (1971).
9. D. L. Judge, G. S. Bloom, and A. S. Morse, Cad. J. Phys. 47, 489, (1969).
10. M. J. Mumma, E. J. Stone, and E. C. Zipf, J. Chem. Phys., 54, 2627, (1971).
11. M. J. Mumma, Ph.D. Thesis
12. J. Ajello, J. Chem. Phys., 55, 3169, (1971).
13. W. Sroka, Z. Naturforsch. 25a, 1434, (1970).
14. R. B. Cairns and J.A.R. Sampson, J. Geophys. Res., 70, 99, (1965).
15. J. E. Mentall and E. P. Gentieu, J. Chem. Phys., 52, 5641, (1970).
16. F. J. Comes and H. O. Wellern, Z. Naturforsch. 23a, 881, (1968).
17. F. J. Comes and U. Wennings, Z. Naturforsch. 25a, 237, (1970).
18. R. E. Huffman, J. C. Larabee and D. Chambers, Appl. Optics, 4, 1145, (1965).

19. J. E. Brimhall and L. A. Page, Nuclear Instruments and Methods, 35, 328, (1965).

20. R. D. Hudson, Reviews of Geophysics and Space Physics, Vol. 9, No. 2 (1971).

21. Possible causes include thermal expansion in the McPherson precision drive screw and lever arm, and/or, variation in the thickness of the lubricant coating on the precision screw.

22. Y. Tanka and M. Ogawa, Canadian Journal of Phys., 40, 897, (1962).

23. J. E. Mentall and H. D. Morgan, J. Chem. Phys. 56, 2271 (1972).

24. J. A. R. Samson, Techniques of Vacuum Ultraviolet Spectroscopy, (John Wiley & Sons, 1967).

25. M. J. Mumma, E. J. Stone, W. L. Borst, and E. C. Zipf, J. Chem. Phys., 57, 68,(1972.)

26. G. Herzberg, "Molecular Spectra and Molecular Structure, Vol. III" 2nd Ed., (Van Nostrand, 1950).

27. E.C.Y. Inn and J. M. Heimerl, J. Atmos., Sci., 28, 838, (1971).

28. M. Krauss, S. R. Mielczarek, D. Newmann, and C. E. Kuyatt, J. Geophys. Res., 76, 3733,(1971).

29. Y. Tanaka, A. S. Jursa, and F. J. LeBlanc, J. Chem. Phys.,5354 (1960).

30. J.F.M. Aarts and F. J. de Heer, J. Chem.Phys. 52, 5354, (1970).

31. This calculation is presently under way in collaboration with J. Herman, R. E. Hartle, and M.J. Mumma and will be reported in the near future.

32. G. E. Thomas, J. Atmos. Sci., 28, 859, (1971).

33. σ_{pd} is particularly suspect below 700Å.

Figure Captions

Figure 1. Schematic diagram of apparatus used to measure $CO(A^1\Pi)$ cross sections.

Figure 2. $CO(A^1\Pi\text{-}X^1\Sigma)$ vibrational intensity distribution. Fig. 2A represents the distribution obtained from 16.69 eV photon impact on CO_2. Fig. 2B represents the distribution obtained from 20 ± 2 eV electron impact on CO_2. Both distributions were obtained with 7.5Å resolution.

Figure 3. Measured CO 4 PG production cross section $\sigma_f(\lambda)$. Shown also are CO_2 photoabsorption, photoionization, and photodissociation cross sections, σ_t, σ_i, σ_{pd} measured by Nakata. Thresholds for the competing dissociation and ionization channels are shown along the top of the figure.

Figure 4. Histogram showing the behavior of the mean of the ratio of the signals generated by the two solar blind photomultipliers observing fluorescence radiation. Each 6 - 12Å wavelength interval represents the average of at least 5000 counts by each tube. S_{BaF_2} refers to the tube preceded by a 1 mm thick BaF_2 window, S_{Bare} to the tube with no window.

Figure 5. Total and dissociation yields for photons on CO_2 to produce $CO(A^1\Pi)$. Fig. 5A was computed on a point for point basis by fitting a curve to Nakata's data and interpolating values for σ_t and σ_{pd} at each wavelength

that a CO 4PG cross section was measured. Fig. 5B was computed by integrating across corresponding features in the σ_t, σ_{pd} and σ_f curves.

TABLE I

λ	$\sigma_f \times 10^{19}$	
635.93	0.32	
637.88	0.31	
639.91	0.42	
641.91	0.40	
643.92	0.43	
645.91	0.61	
647.90	0.62	
649.88	0.42	
651.86	0.35	
653.87	0.27	
655.85	0.59	
657.85	0.41	
659.85	0.18	
661.86	0.33	
663.90	0.84	
665.89	0.44	
667.93	0.34	
669.92	0.25	
671.89	0.34	
673.90	0.45	
675.14	0.48	
676.14	0.47	
677.13	0.56	
678.11	0.73	
679.10	0.57	
680.12	1.02	
681.11	0.91	
682.10	1.43	
683.10	2.34	
684.09	1.69	
685.10	1.67	
686.12	5.34	
687.12	6.52	
688.12	6.30	
689.13	5.83	
690.14	8.08	- H(s) 11,0
691.15	7.90	- H(s) 10,0
692.15	10.20	- H(s) 9,0
693.15	2.70	
694.14	12.22	- H(s) 8,0
695.15	3.38	
696.16	3.46	
697.14	3.78	
698.14	4.15	
699.13	3.81	
700.35	16.33	- H(s) 6,0
701.35	2.73	
702.33	5.62	
703.31	4.39	
704.30	4.10	
705.32	4.65	
706.32	4.74	
707.29	6.11	
708.29	3.87	
709.29	4.85	
710.31	16.27	- H(d) 5,0 OR T-0 5,5
711.32	6.34	OR 7,3
712.33	6.03	
713.32	4.19	
714.33	5.51	- T-0 6,3
715.35	5.84	
716.35	7.40	
717.35	11.45	
718.35	9.35	
719.35	8.60	
720.36	9.74	- T-0 6,2
721.35	7.72	
722.34	7.32	
723.33	10.59	
724.33	5.59	
725.33	8.20	
726.32	29.69	- H(d) 4,0 OR T-0 6,1
727.31	16.13	- T-0 5,2 OR 7,0
728.31	6.92	
729.30	18.23	- T-0 4,4
730.32	7.09	
731.32	5.94	
732.30	5.02	

λ	$\sigma_f \times 10^{19}$	
636.40	0.32	
638.41	0.45	
640.41	0.50	
642.41	0.46	
644.41	0.53	
646.39	0.41	
648.39	0.34	
650.35	0.57	
652.36	0.40	
654.35	0.39	
656.35	0.37	
658.37	0.55	
660.36	0.25	
662.38	0.48	
664.40	0.56	
666.39	0.35	
668.42	0.36	
670.41	0.51	
672.38	0.64	
674.38	0.57	
675.38	0.52	
676.38	0.58	
677.37	0.68	
678.35	0.58	
679.35	0.72	
680.38	0.98	
681.35	1.10	
682.34	1.69	
683.35	2.05	
684.35	1.22	
685.35	1.48	
686.37	6.44	
687.37	5.93	
688.38	6.46	
689.39	5.39	
690.40	3.81	
691.40	3.18	
692.40	7.36	
693.40	2.05	
694.39	9.60	
695.41	2.94	
696.40	6.78	
697.37	3.61	
698.38	2.99	
699.37	4.19	
700.58	7.96	
701.58	3.44	
702.58	4.65	
703.56	3.57	
704.55	5.53	- T-0 5,6 OR 7,4
705.58	4.20	
706.57	4.70	
707.55	4.65	
708.55	3.72	
709.55	5.98	
710.56	14.33	
711.58	7.45	
712.58	5.47	
713.58	3.59	
714.59	4.86	
715.60	8.59	- T-0 ∞,0
716.60	6.25	
717.60	12.88	- H(s) 4,0 OR T-0 4,6
718.60	10.76	
719.60	7.58	
720.62	8.08	
721.60	11.31	- T-0 7,1 OR 5,3
722.59	6.59	
723.58	10.81	- T-0 4,5
724.58	4.64	
725.58	10.22	
726.57	27.14	
727.56	14.55	
728.54	6.95	
729.54	13.79	
730.57	5.94	
731.56	5.26	
732.54	4.80	

λ	$\sigma_f \times 10^{19}$	
636.88	0.25	
638.91	0.22	
640.91	0.30	
642.92	0.45	
644.92	0.50	
646.89	0.35	
648.89	0.45	
650.88	0.55	
652.85	0.27	
654.86	0.52	
656.84	0.38	
658.85	0.44	
660.86	0.40	
662.87	0.36	
664.90	0.62	
666.90	0.49	
668.91	0.59	
670.92	0.47	
672.91	0.41	
674.65	0.46	
675.63	0.46	
676.62	0.63	
677.60	0.52	
678.59	0.70	
679.60	0.85	
680.62	0.77	
681.60	1.11	
682.58	2.30	
683.59	1.94	
684.59	1.45	
685.61	1.55	
686.62	7.13	
687.62	6.46	
688.63	6.21	
689.65	4.36	
690.66	4.24	
691.65	2.35	
692.66	5.03	
693.65	4.28	
694.65	5.43	
695.67	2.40	
696.65	9.41	- H (s) 7,0
697.63	4.63	
698.63	2.51	
699.85	4.64	
700.83	3.90	
701.82	4.62	
702.81	4.04	
703.80	3.50	
704.80	5.33	
705.82	4.13	
706.81	6.21	
707.79	4.15	
708.79	4.17	
709.80	9.75	
710.80	10.07	
711.82	7.57	- T-0 4,7
712.83	4.78	
713.83	3.70	
714.84	4.92	
715.85	10.04	- T-0 5,4
716.85	6.36	
717.85	11.30	
718.85	11.59	- T-0 8,1
719.85	8.03	
720.87	6.46	
721.85	10.35	
722.84	5.96	
723.83	8.64	
724.83	5.20	
725.83	13.17	
726.81	16.65	
727.81	9.56	
728.80	9.14	
729.80	10.94	
730.81	6.21	
731.80	4.92	
732.78	5.20	

λ	$\sigma_f \times 10^{19}$	
637.40	0.25	
639.41	0.42	
641.40	0.50	
643.42	0.62	
645.41	0.51	
647.39	0.38	
649.37	0.32	
651.36	0.37	
653.35	0.39	
655.37	0.87	
657.35	0.51	
659.35	0.45	
661.37	0.42	
663.39	0.36	
665.39	0.53	
667.41	0.36	
669.40	0.60	
671.39	0.29	
673.40	0.45	
674.90	0.37	
675.89	0.48	
676.88	0.62	
677.86	0.59	
678.85	0.63	
679.86	0.85	
680.85	1.03	
681.84	1.05	
682.84	2.11	
683.84	1.58	
684.84	1.30	
685.86	3.07	- H(s) ∞,0
686.87	6.34	
687.85	6.92	
688.88	6.01	
689.90	5.93	
690.90	7.66	
691.90	4.41	
692.91	3.88	
693.90	11.25	
694.91	4.50	
695.92	2.51	
696.90	5.77	
697.88	6.21	- H(d) 7,0 OR T-0 6,6
698.88	2.85	
700.10	10.37	
701.09	2.91	
702.07	6.32	- H(d) 6,0 OR T-0 8,4
703.06	4.11	
704.05	3.63	
705.06	4.93	
706.06	4.47	
707.05	8.12	- H(s) 5,0
708.04	3.94	
709.04	4.73	
710.05	14.08	- T-0 ∞,1
711.06	6.13	
712.07	6.58	
713.06	4.73	
714.07	4.78	
715.09	4.94	
716.10	8.15	
717.09	7.70	
718.10	9.68	
719.10	9.80	
720.10	9.84	
721.12	5.65	
722.10	7.58	
723.10	7.32	
724.09	7.25	
725.09	6.73	
726.09	17.95	
727.07	11.88	
728.07	6.74	
729.05	15.59	
730.07	9.17	
731.07	6.54	
732.05	4.63	
733.04	5.86	

TABLE I

λ	$\sigma_f \times 10^{19}$	
733.30	9.56	
734.30	16.61	
735.31	22.09	
736.31	7.21	
737.33	3.86	
738.33	2.69	
739.60	6.39	T-O 5,0
741.60	18.74	T-O 4,2
743.62	4.89	
745.60	11.60	?
747.59	15.74	T-O 4,1
748.78	10.56	
750.03	4.01	
751.03	6.31	
752.00	21.84	
752.99	32.92	
754.24	18.93	T-O 4,0 OR 3,5
755.25	11.00	
756.60	5.54	
759.10	7.79	
761.10	13.43	
763.13	8.49	
765.14	12.43	
767.15	18.07	T-O 3,3
769.15	8.55	
771.14	13.71	P 2-0
773.15	18.33	
775.12	11.92	
777.10	10.21	
779.10	10.58	
781.09	11.86	
783.10	9.90	
785.10	6.97	
787.11	11.21	T-O 3,0
789.14	10.43	
791.13	6.97	
793.16	7.35	
795.14	9.73	
797.14	6.78	
799.13	6.00	
801.12	8.19	
803.10	6.49	
805.05	4.74	
807.05	5.92	P I
809.06	5.12	
811.07	4.27	
813.08	4.31	
815.11	3.60	
817.10	2.85	
819.12	2.47	
821.10	2.47	
823.08	1.70	
825.10	1.30	
827.04	2.20	P I
829.06	1.23	
831.05	1.18	
833.03	1.11	
835.07	1.07	
837.08	1.27	
839.09	1.24	
841.11	1.54	
843.10	1.50	
845.12	1.53	
846.78	1.57	
848.76	1.74	
850.76	1.71	
852.72	1.80	
854.74	2.02	
856.71	2.38	
858.71	2.18	
860.73	2.30	
862.74	1.94	
864.76	2.44	
866.76	2.81	
868.78	2.48	
870.78	3.72	
872.77	3.48	
874.77	4.45	
876.24	5.55	

λ	$\sigma_f \times 10^{19}$	
733.54	12.85	T-O 5,1
734.55	26.24	?
735.55	12.21	
736.56	6.03	
737.58	2.80	
738.58	2.76	
740.10	4.12	
742.10	11.66	
744.12	2.88	
746.10	8.68	
748.10	12.59	
749.03	8.42	
750.29	4.49	
751.29	7.90	
752.26	45.46	
753.25	19.50	
754.49	15.60	
755.51	9.22	
757.10	4.39	
759.60	7.25	
761.60	10.31	
763.65	8.21	
765.65	8.30	
767.66	14.11	
769.66	8.68	
771.64	12.73	
773.64	22.29	T-O 3,2
775.62	12.29	
777.59	10.94	P 1-0
779.60	14.25	
781.59	11.75	
783.59	9.20	
785.60	6.88	
787.62	9.99	
789.65	9.27	
791.65	6.69	
793.66	7.39	
795.65	9.92	P I
797.64	6.59	
799.61	6.27	
801.60	8.02	
803.56	6.12	
805.56	4.84	
807.53	5.54	
809.57	4.78	
811.57	3.95	
813.58	4.59	P I
815.60	3.42	
817.60	2.73	
819.62	2.81	
821.60	2.45	
823.60	1.65	
825.59	1.41	
827.55	1.92	
829.55	1.14	
831.55	1.32	
833.54	1.14	
835.56	1.16	
837.58	1.13	
839.59	1.31	
841.61	1.53	
843.62	1.58	
845.61	1.48	
847.26	1.74	
849.26	1.59	
851.24	1.85	
853.21	1.64	
855.21	1.76	
857.21	2.28	
859.21	2.20	
861.23	2.26	
863.26	2.80	
865.26	2.51	
867.28	2.98	
869.28	3.00	
871.27	3.78	
873.26	3.54	
875.25	4.11	
876.74	4.88	

λ	$\sigma_f \times 10^{19}$	
733.78	10.85	
734.79	23.38	T-O 4,3
735.80	9.65	
736.82	5.30	
737.81	2.47	
738.60	2.54	
740.60	6.09	
742.60	10.60	
744.61	3.13	
746.59	5.73	
748.28	12.75	
749.27	6.88	
750.52	5.05	
751.52	10.67	
752.50	119.99	H (s) 3,0
753.50	10.99	
754.73	15.41	
755.60	8.45	
757.59	5.26	
760.10	10.52	
762.12	10.24	
764.14	9.47	
766.14	9.62	
768.15	11.68	
770.15	9.25	
772.14	8.77	
774.13	16.50	
776.12	11.27	
778.10	10.46	
780.11	17.45	T-O 3,1
782.10	12.04	
784.09	8.41	
786.10	7.51	
788.13	9.59	
790.13	8.02	
792.15	6.89	
794.14	7.77	
796.14	8.45	
798.15	5.85	
800.12	7.44	
802.11	7.01	
804.06	5.86	
806.06	5.20	
808.04	5.23	
810.07	4.51	
812.09	5.26	
814.09	4.28	
816.11	3.49	
818.11	2.46	
820.11	3.12	P I
822.10	2.36	
824.09	1.73	
826.07	1.53	
828.04	1.43	
830.04	1.27	
832.05	1.25	
834.06	1.19	
836.07	1.14	
838.09	1.19	
840.10	1.40	
842.10	1.66	
844.12	1.43	
846.10	1.61	
847.77	1.57	
849.76	1.78	
851.74	1.84	
853.74	1.98	
855.72	1.80	
857.71	2.00	
859.73	2.42	
861.73	2.07	
863.75	2.32	
865.77	2.59	
867.77	2.74	
869.79	2.81	
871.77	3.19	
873.78	4.24	
875.76	3.40	
877.22	4.14	

λ	$\sigma_f \times 10^{19}$	
734.04	10.24	
735.05	21.76	
736.06	8.05	
737.07	4.99	
738.07	2.43	
739.09	2.95	
741.10	12.31	
743.12	6.20	
745.12	7.21	
747.10	5.08	
748.53	12.34	
749.51	5.46	
750.77	5.64	
751.75	12.58	
752.74	72.48	
753.99	18.66	
754.99	11.30	
756.10	6.28	
758.10	7.60	P 4-0
760.60	14.07	T-O 3,4
762.63	9.28	
764.65	14.12	H (d) 3,0 P 3-0
766.65	14.62	
768.67	9.18	
770.65	10.66	
772.65	11.59	
774.61	13.91	
776.60	10.32	
778.59	8.71	
780.60	14.98	
782.59	11.92	
784.59	8.12	
786.61	9.07	
788.65	10.63	
790.65	7.54	
792.66	7.23	
794.65	9.06	
796.63	8.05	
798.63	6.04	
800.62	8.68	P I
802.59	6.55	
804.56	5.18	
806.55	5.91	
808.55	4.76	
810.56	4.50	
812.58	4.10	
814.60	4.14	
816.60	3.16	
818.63	2.37	
820.61	2.82	
822.60	1.76	
824.60	1.48	
826.56	1.83	
828.56	1.16	
830.54	1.10	
832.54	1.20	
834.56	1.25	P I
836.57	1.20	
838.59	1.28	
840.61	1.45	
842.60	1.52	
844.62	1.50	
846.60	1.67	
848.27	1.87	
850.25	1.72	
852.21	1.92	
854.23	1.94	
856.21	1.82	
858.21	2.25	
860.22	2.36	
862.24	2.26	
864.26	2.32	
866.27	2.55	
868.28	2.59	
870.28	2.85	
872.26	3.88	
874.26	4.01	
876.24	5.55	
877.75	6.37	

TABLE I

λ	$\sigma_f \times 10^{19}$	λ	$\sigma_f \times 10^{19}$	λ	$\sigma_f \times 10^{19}$	λ	$\sigma_f \times 10^{19}$
878.22	7.27	878.75	5.44	879.23	5.91	879.75	8.03
880.22	5.54	880.73	6.00	881.21	10.54	881.71	7.12
882.21	8.23	882.73	8.04	883.10	7.60	883.35	6.96
883.60	6.80	883.85	7.03	884.11	8.00	884.37	9.31
884.62	11.14	884.87	10.82	885.13	9.21	885.38	8.05
885.63	8.61	885.88	8.22	886.13	9.39	886.39	8.45
886.63	9.07	886.88	8.50	887.13	8.48	887.39	9.23
887.63	9.41	887.87	9.93	888.13	10.77	888.39	11.20
888.65	11.64	888.88	12.14	889.14	12.14	889.39	12.51
889.65	12.89	889.90	13.18	890.15	13.53	890.41	14.62
890.67	15.33	890.91	15.76	891.16	15.55	891.41	14.99
891.66	13.61	891.91	12.98	892.15	13.52	892.40	14.55
892.65	15.17	892.91	16.40	893.15	17.22	893.40	17.04
893.66	16.41	893.91	15.11	894.15	14.79	894.40	15.40
894.66	17.40	894.92	18.05	895.16	18.28	895.42	16.83
895.67	16.60	895.92	16.25	896.16	16.35	896.40	16.61
896.65	17.24	896.91	18.41	897.15	18.62	897.39	17.90
897.64	16.95	897.90	17.63	898.15	18.79	898.39	18.47
898.63	18.10	898.88	18.07	899.13	18.74	899.38	20.04
899.62	20.71	899.89	22.57	900.14	24.28	900.38	27.64
900.65	31.61	900.90	32.04	901.15	30.13	901.38	27.08
901.62	24.78	901.87	21.56	902.12	19.38	902.36	18.41
902.60	19.26	902.86	17.90	903.12	17.81	903.37	20.21
903.60	23.59	903.87	23.38	904.12	20.69	904.37	18.91
904.61	18.31	904.87	19.23	905.14	19.63	905.38	18.80
905.62	17.08	905.87	15.60	906.12	16.03	906.37	16.34
906.61	15.75	906.86	14.72	907.11	13.95	907.35	13.69
907.60	13.37	907.85	12.30	908.10	11.55	908.35	11.16
908.59	10.92	908.84	10.26	909.10	10.49	909.35	11.04
909.60	11.40	909.86	11.40	910.12	10.35	910.37	9.93
910.62	10.36	910.88	10.57	911.13	11.61	911.38	10.42
911.62	9.55	911.87	9.00	912.13	8.52	912.38	7.88
912.63	7.45	912.87	6.68	913.13	5.84	913.39	5.49
913.65	5.50	913.89	6.19	914.14	5.63	914.40	5.98
914.66	6.43	914.91	6.82	915.15	6.49	915.41	6.12
915.67	6.80	915.91	6.27	916.16	5.24	916.41	4.29
916.66	3.83	916.91	4.20	917.15	4.78	917.17	4.89
917.69	4.79	918.18	4.17	918.69	4.43	919.17	4.61
919.68	2.18	920.18	2.27	920.68	2.08	921.16	1.44
921.67	1.58	922.16	1.31	922.67	0.95	923.17	0.86
923.67	0.52	924.16	0.29	924.64	0.22	925.14	0.07
925.64	0.06	925.99	0.00	999.00	0.00	0.00	0.00

TABLE II

Quantity	Approximate % Error
$\sigma_t(CO_2)$	5 - 15% †
$Q_f(1216)/\bar{Q}$	5 - 25%*
$Q_s(\lambda)/Q_s(839)$	6%
$S_f(CO_2)$	2 - 4%
$S_s(CO_2)$	6%
$N(CO_2)$	5%
X-L	3%
$\sigma_t(H_2)$	10%
$S_f(H_2)$	1.5%
$S_s(H_2)$	3%
$N(H_2)$	5%
λ	±.25Å
σ_{pd}	30%

† includes Nakata's quoted errors plus an additional uncertainty due to possible error in wavelength scale.

*25% figure holds only near thresholds for $CO(A^1\Pi\ v'=0)$.

TABLE CAPTIONS

Table I. Tabulated CO 4PG cross sections. Shown also are the Rydberg identifications[23,29] discussed in the text. eg: H(s)4,0 refers to the n=4 member of the v'=0 Henning sharp series, T-O 3,4 refers to the n=3 member of the v'=4 Tanaka-Ogawa series etc.

Table II. Summary of the uncertainties present in the CO 4PG cross section measurements.

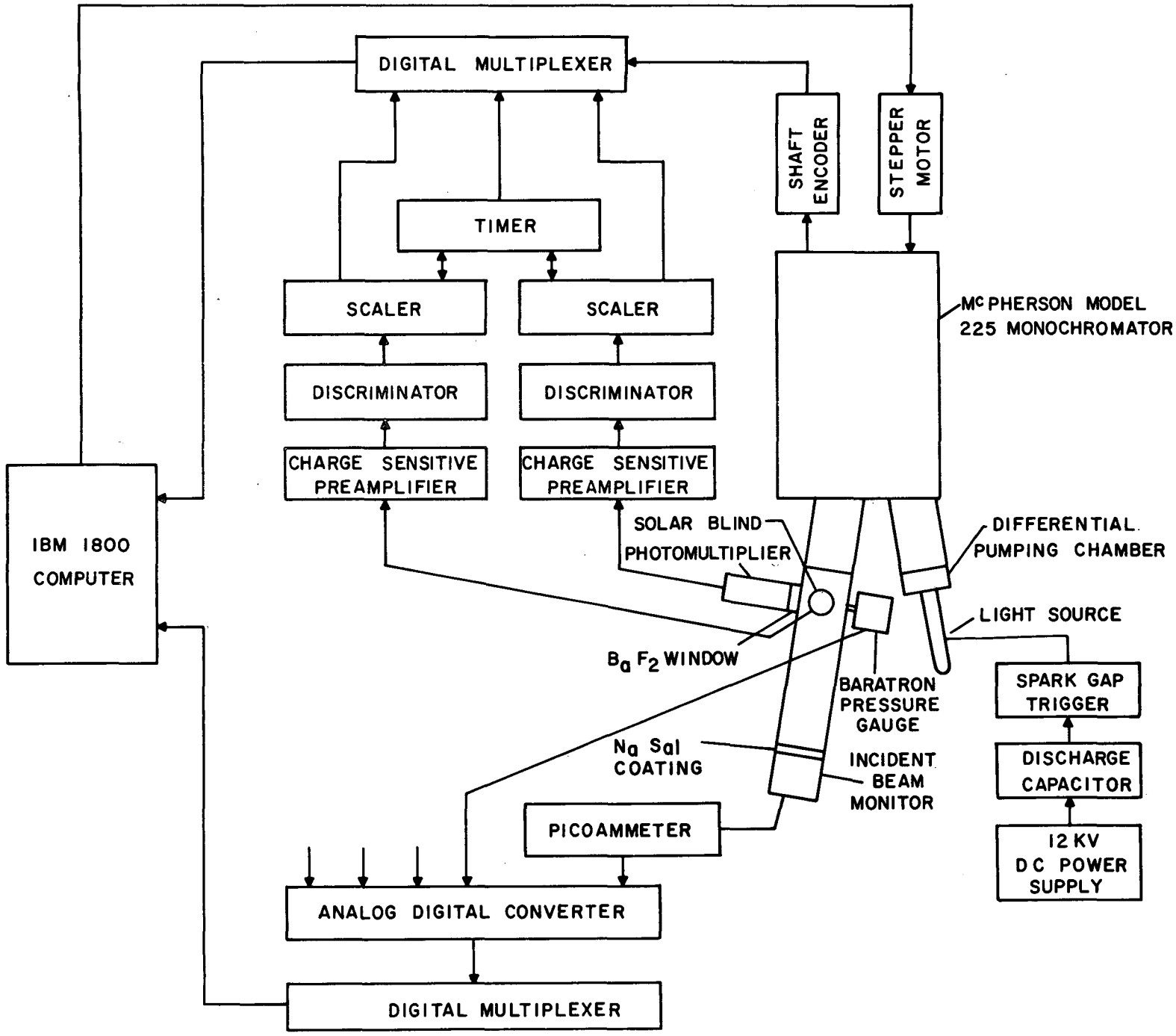
DIGITAL MULTIPLEXER
SHAFT ENCODER
STEPPER MOTOR
TIMER
SCALER
SCALER
McPHERSON MODEL 225 MONOCHROMATOR
DISCRIMINATOR
DISCRIMINATOR
CHARGE SENSITIVE PREAMPLIFIER
CHARGE SENSITIVE PREAMPLIFIER
IBM 1800 COMPUTER
SOLAR BLIND PHOTOMULTIPLIER
DIFFERENTIAL PUMPING CHAMBER
LIGHT SOURCE
$B_a F_2$ WINDOW
BARATRON PRESSURE GAUGE
SPARK GAP TRIGGER
N_a Sal COATING
INCIDENT BEAM MONITOR
DISCHARGE CAPACITOR
PICOAMMETER
12 KV DC POWER SUPPLY
ANALOG DIGITAL CONVERTER
DIGITAL MULTIPLEXER

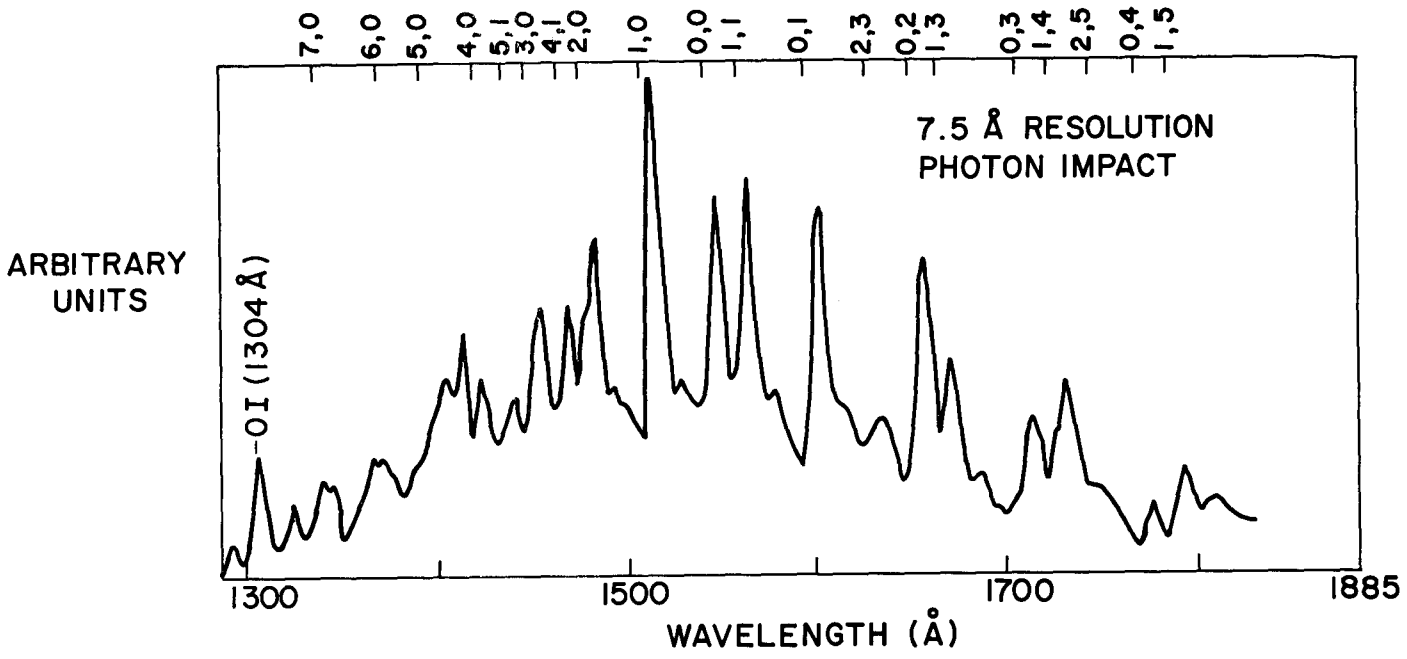
7,0
6,0
5,0
4,0
5,1
3,0
4,1
2,0
1,0
0,0
1,1
0,1
2,3
0,2
1,3
0,3
1,4
2,5
0,4
1,5
7.5 Å RESOLUTION
PHOTON IMPACT
ARBITRARY
UNITS
OI (1304 Å)
1300
1500
1700
1885
WAVELENGTH (Å)

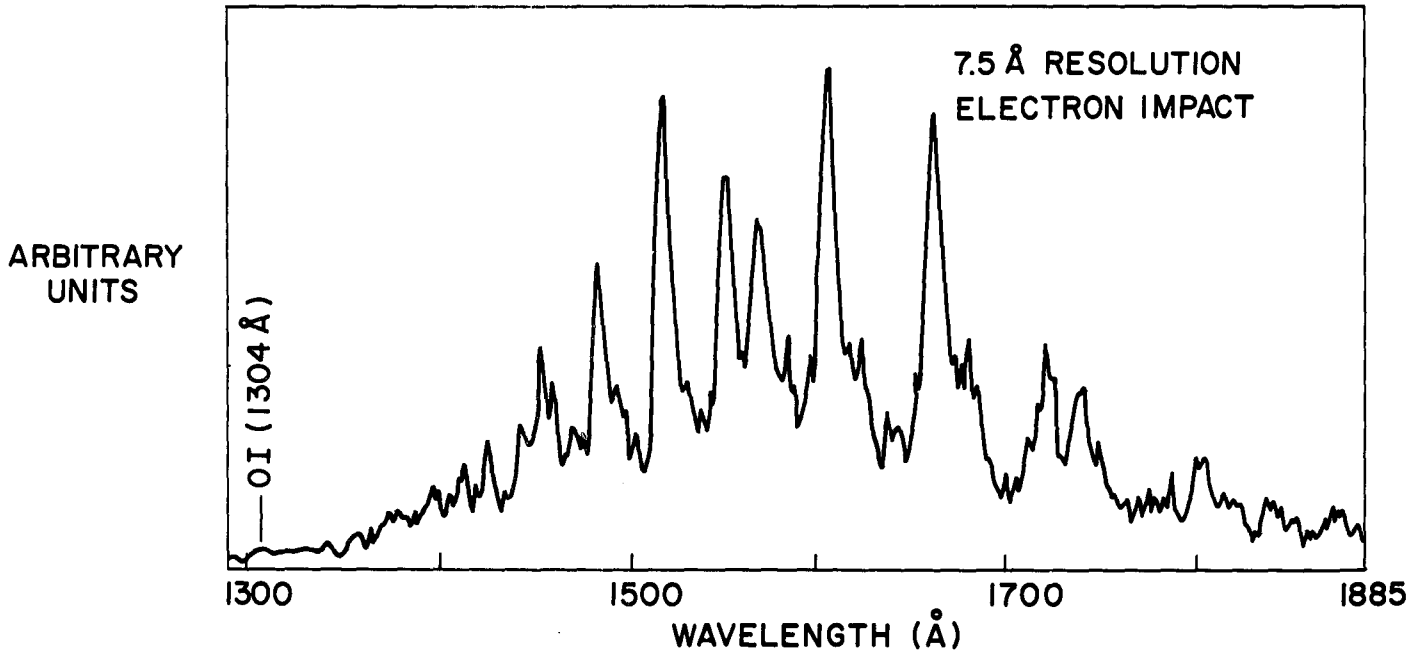
7.5 Å RESOLUTION
ELECTRON IMPACT
ARBITRARY
UNITS
OI (1304 Å)
1300
1500
1700
1885
WAVELENGTH (Å)

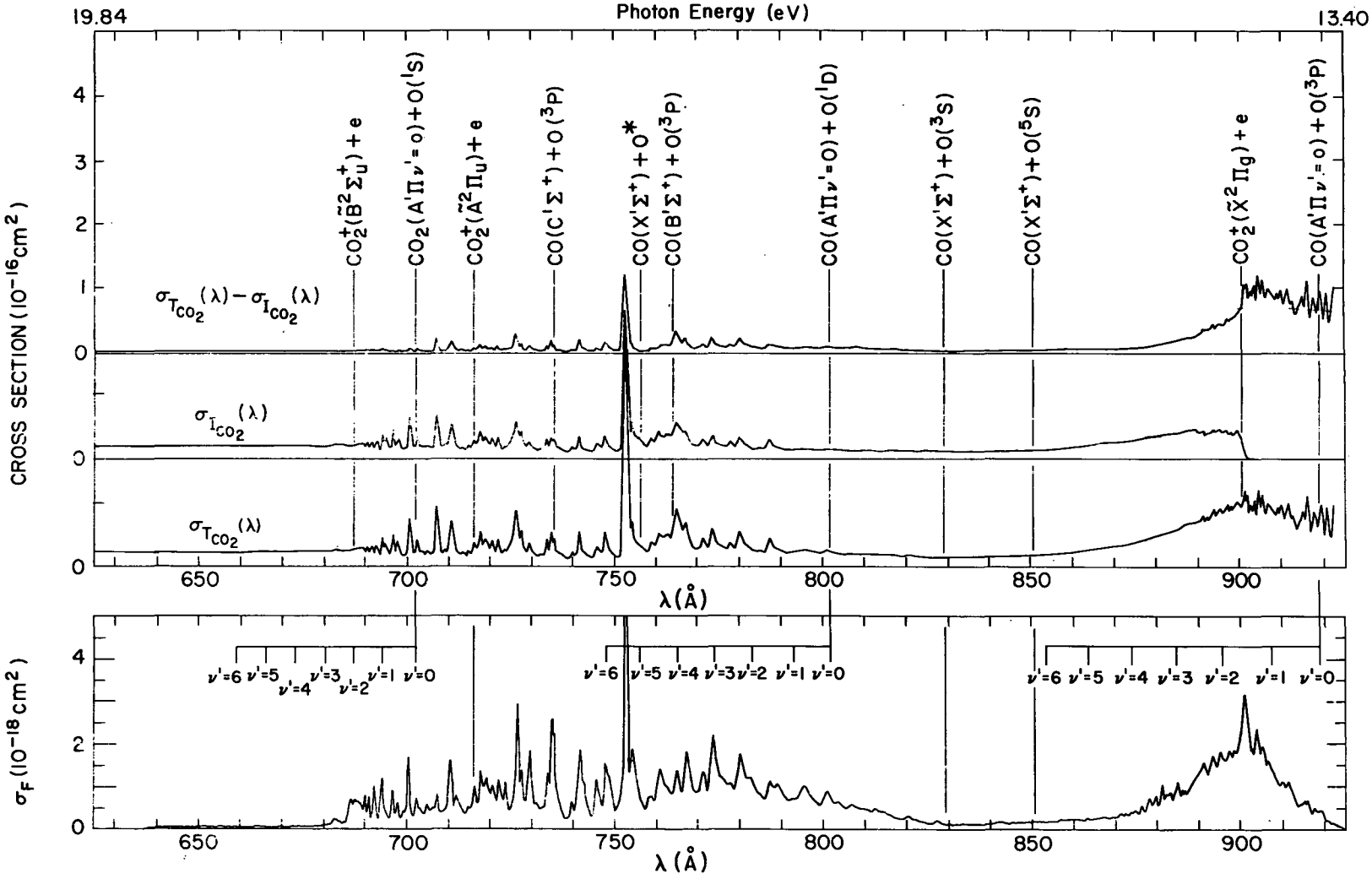
19.84
Photon Energy (eV)
13.40
CROSS SECTION (10^{-16}cm^2)
$\sigma_{T_{CO_2}}(\lambda) - \sigma_{I_{CO_2}}(\lambda)$
$\sigma_{I_{CO_2}}(\lambda)$
$\sigma_{T_{CO_2}}(\lambda)$
$CO_2^+(\tilde{B}^2\Sigma_u^+) + e$
$CO_2(A'\Pi\,\nu'=0) + O(^1S)$
$CO_2^+(\tilde{A}^2\Pi_u) + e$
$CO(C'\Sigma^+) + O(^3P)$
$CO(X'\Sigma^+) + O^*$
$CO(B'\Sigma^+) + O(^3P)$
$CO(A'\Pi\,\nu'=0) + O(^1D)$
$CO(X'\Sigma^+) + O(^3S)$
$CO(X'\Sigma^+) + O(^5S)$
$CO_2^+(\tilde{X}^2\Pi_g) + e$
$CO(A'\Pi\,\nu'=0) + O(^3P)$
0
1
2
3
4
650
700
750
800
850
900
λ(Å)
σ_F (10^{-18}cm^2)
$\nu'=6$ $\nu'=5$ $\nu'=4$ $\nu'=3$ $\nu'=2$ $\nu'=1$ $\nu'=0$
$\nu'=6$ $\nu'=5$ $\nu'=4$ $\nu'=3$ $\nu'=2$ $\nu'=1$ $\nu'=0$
$\nu'=6$ $\nu'=5$ $\nu'=4$ $\nu'=3$ $\nu'=2$ $\nu'=1$ $\nu'=0$
λ (Å)

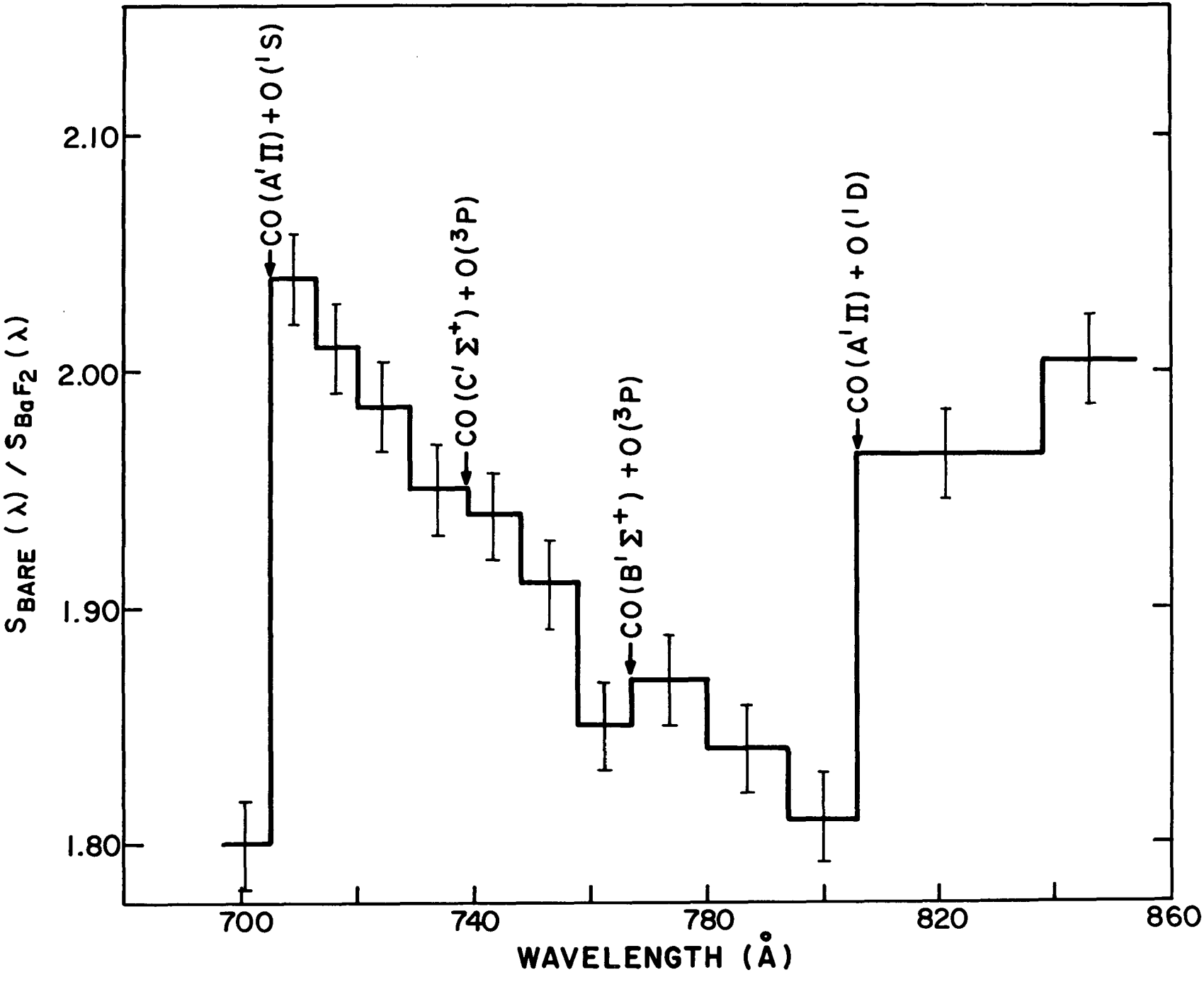
CO (A'Π) + O('S)
CO (C'Σ+) + O(3P)
CO(B'Σ+) + O(3P)
CO (A'Π) + O('D)
2.10
2.00
1.90
1.80
700
740
780
820
860
WAVELENGTH (Å)
SBARE (λ) / SBaF2 (λ)

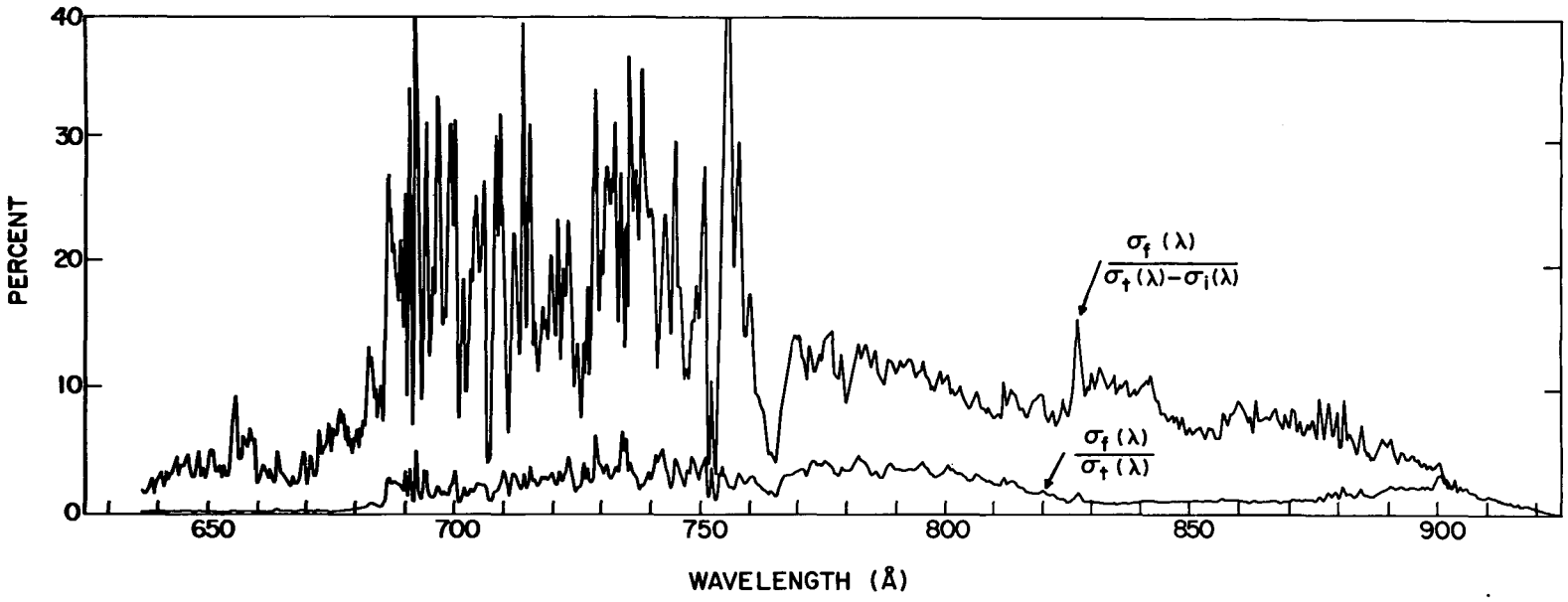

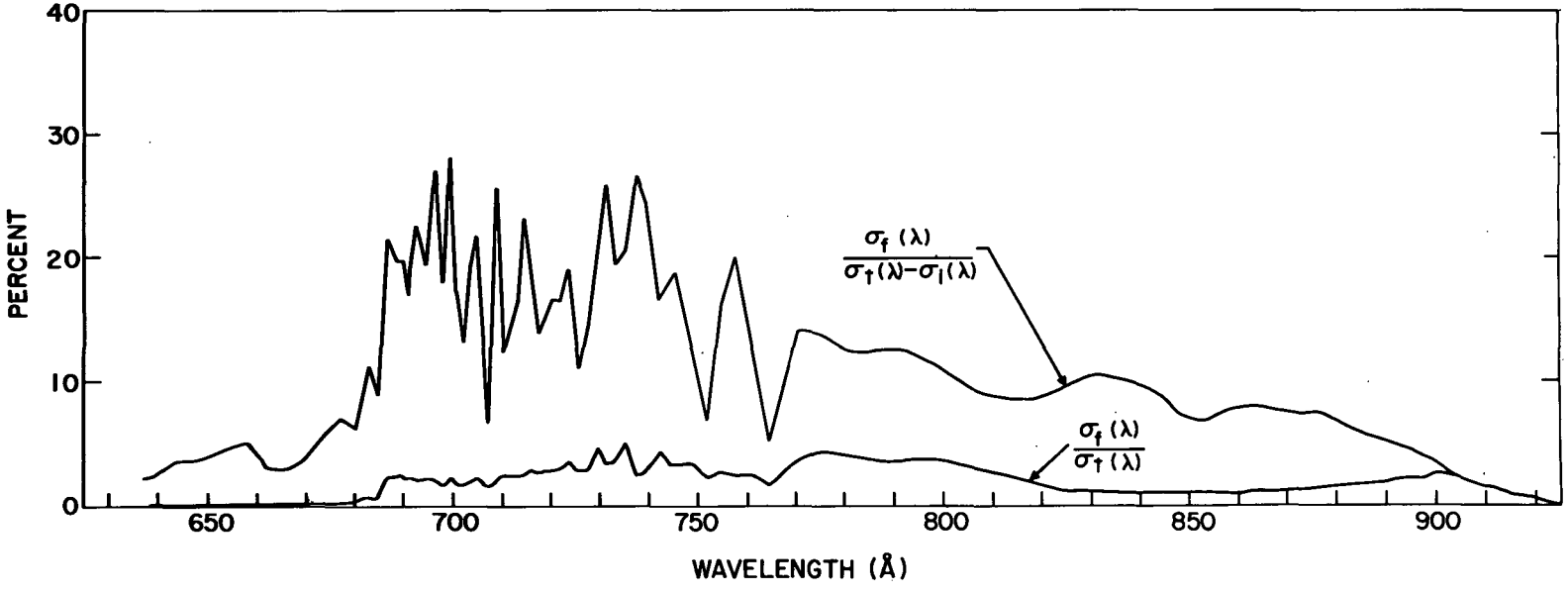

* U.S. GOVERNMENT PRINTING OFFICE: 1972—735-963/206